RSC Advances

PAPER

View Article Online
View Journal | View Issue



Cite this: *RSC Adv.*, 2022, **12**, 17182

# Manganese oxide nanorod catalysts for low-temperature selective catalytic reduction of NO with $NH_3$

Yifan Wang, Yanli Wang,* Zhenkai Kong, Ying Kang and Liang Zhan *

$MnO_x$ nanorod catalysts were successfully synthesized by two different preparation methods using porous $SiO_2$ nanorods as the template and investigated for the low-temperature selective catalytic reduction (SCR) of NO with $NH_3$. The catalysts were characterized by scanning electron microscopy, transmission electron microscopy, nitrogen adsorption, X-ray diffraction, X-ray photoelectron spectroscopy, and $NH_3$ temperature-programmed desorption. The results show that the obtained $MnO_x$-P nanorod catalyst prepared by redox precipitation method exhibits higher NO removal activity than that prepared by the solvent evaporation method in the low temperature range of 100–180 °C, where about 98% NO conversion is achieved over $MnO_x$(0.36)-P nanorods. The reason is mainly attributed to $MnO_x$(0.36)-P nanorods possessing unique flower-like morphology and mesoporous structures with high pore volume, which facilitates the exposure of more active sites of $MnO_x$ and the adsorption of reactant gas molecules. Furthermore, there is a lower crystallinity of $MnO_x$, higher percentage of $Mn^{4+}$ species and a large amount of strong acid sites on the surface. These factors contribute to the excellent low-temperature SCR activity of $MnO_x$(0.36)-P nanorods.

Received 8th September 2021
Accepted 31st March 2022

DOI: 10.1039/d1ra06758c

rsc.li/rsc-advances



## 1. Introduction

Nitrogen oxides ($NO_x$) are considered to be one of the main air pollutants, which can cause great harm to the ecological environment and human health. Therefore, it is urgent to control the emissions of $NO_x$. The selective catalytic reduction (SCR) of NO with $NH_3$ has been proven to be the most effective technology for the removal of $NO_x$. Commercial SCR catalysts, $V_2O_5$–$WO_3/TiO_2$ and $V_2O_5$–$MoO_3/TiO_2$ catalysts have shown high activity of NO removal, and these catalysts must be used in the temperature range of 350–450 °C.[1,2] To satisfy the high operating temperature, the SCR unit needs to be placed upstream of the electrostatic precipitator and desulfurization devices, resulting in the deactivation of catalysts because of high concentration of dust and $SO_2$ in the flue gases. In order to overcome the disadvantages of these $V_2O_5/TiO_2$ based catalysts, researchers have paid much attentions on developing efficient low-temperature SCR catalysts, which can be placed downstream of the desulfurizer and electrostatic precipitators without the need for reheating of flue gases.[3–5]

Various transition metal oxide catalysts have been found to be active in the $NH_3$-SCR reaction. Among them, manganese oxide ($MnO_x$) catalysts exhibit excellent low temperature-SCR activities due to their variable valence states and high redox properties.[6,7] In addition, it has been demonstrated that the specific surface area and crystallinity of $MnO_x$ have also great influence on their SCR activities.[8] Furthermore, it has been reported that the morphologies of the catalysts significantly influence their properties and catalytic performance.[9–11] Recently, mesoporous materials have attracted extensive attention owing to their large specific surface area, highly ordered mesoporous structure, which are advantageous to the generation of abundant active sites and mass transport of gas molecules. In particular, mesoporous metal oxides combine the advantages of both metal oxides and mesoporous structure in comparison with nanoparticles, which have found applications in various fields, such as electrode materials, gas sensors and adsorption, catalysis, *etc.*[12–14] For instance, Gao *et al.*[15] reported a three-dimensional (3D) mesoporous $MnO_2$ prepared using KIT-6 as a template, which showed much higher SCR activity than mesoporous $MnO_2$ templated from SBA-15 or MCM-41, maintaining NO conversion of 100% in the temperature range of 75–275 °C, because of the special 3D mesostructure. Tian *et al.*[16] studied $MnO_2$ nanorods exhibited higher NO conversion than $MnO_2$ nanotubes and nanoparticles, and found that the higher SCR activity of $MnO_2$ nanorods may be mainly attributed to lower crystallinity, more lattice oxygen, higher reducibility, and more amount of strong acid sites. Therefore, controlled synthesis of $MnO_x$ catalysts with different morphologies is very effective way to improve their SCR activities. However, there are still many challenges.

*State Key Laboratory of Chemical Engineering, Key Laboratory for Specially Functional Polymers and Related Technology of Ministry of Education, Shanghai Key Laboratory of Multiphase Materials Chemical Engineering, East China University of Science and Technology, Shanghai 200237, China. E-mail: zhanliang@ecust.edu.cn; Fax: +86 21 64252914; Tel: +86 21 64252924*

In this work, we synthesized a series of $MnO_x$ nanorods catalysts using porous $SiO_2$ nanorods as template through two different preparation methods. The activities of these $MnO_x$ nanorods catalysts for SCR of NO at low temperatures were evaluated. The effect of Mn loading on SCR activities of $MnO_x$ nanorods catalysts at different temperatures were also investigated. The catalysts were characterized to understand the structure and morphologies of $MnO_x$ nanorods catalysts as well as their relationship with catalytic activity. The results are of importance for better understanding of low temperature SCR reaction on nanostructured $MnO_x$ catalysts and beneficial to promote the development of NO removal technology from flue gases.

## 2. Experimental

### 2.1 Catalyst preparation

All the chemical reagents used were analytical grade. $MnO_x$ nanorods catalysts were prepared by two-step process. Firstly, the porous $SiO_2$ nanorods template was synthesized according to the previously reported procedure.[17] Secondly, $MnO_x$ nanorods catalysts were prepared by two different methods using the porous $SiO_2$ nanorods as template. Detailed preparation methods were the following:

**2.1.1 Redox precipitation method (P).** A series of $MnO_x$ nanorods catalysts were synthesized by the redox precipitation method using $KMnO_4$ as oxidant and manganese acetate as reductant, respectively. In a typical synthesis, a certain amount of the as-synthesized porous $SiO_2$ nanorods was initially dispersed in 50 mL deionized water by ultrasonic treatment, subsequently appropriate amount of manganese acetate was slowly added to the above solution. After stirring for 6 h, the solution of $KMnO_4$ containing 40 mL deionized water was slowly added to the above mixture, and continuously stirred for 12 h. The main reaction between $Mn(CH_3COO)_2$ and $KMnO_4$ is expressed by the following equation: ($3Mn^{2+} + 2MnO_4^- + 2H_2O \rightarrow 5MnO_2 + 4H^+$). Then, the obtained product was collected by filtration, and washing several times with deionized water, and then drying at 110 °C for 12 h. Finally, the $SiO_2$@$MnO_x$ was treated with 2 M NaOH solution at 80 °C to remove the $SiO_2$ nanorods template, followed by centrifugation and washing with deionized water several times, drying at 110 °C for 12 h. The resultant catalysts are labeled as $MnO_x$($y$)-P nanorods, where $y$ represents the mass ratio of Mn to $SiO_2$ nanorods template, and P represents the redox precipitation method.

**2.1.2 Solvent evaporation method (E).** For comparison, the $MnO_x$ nanorods catalysts were also synthesized by the solvent evaporation method using manganese acetate as the precursor. A certain amount of the as-synthesized porous $SiO_2$ nanorods was initially dispersed in 40 mL ethanol by ultrasonic treatment. Subsequently, appropriate amount of manganese acetate was slowly added to the above solution, and stirred for 2 h. Then, the mixture was heated up to 50 °C to evaporate the ethanol. The obtained product was dried at 80 °C for 12 h, followed by calcination at 400 °C for 3 h in air atmosphere. Finally, the $SiO_2$ nanorods template was removed with 2 M NaOH solution at 80 °C, then centrifugation, washing with deionized water several times and drying at 110 °C for 12 h. The resultant catalysts are labeled as $MnO_x$($y$)-E nanorods, where $y$ represents the mass ratio of Mn to $SiO_2$ nanorods template, and E represents the solvent evaporation method.

### 2.2 Activity test

NO removal activity tests were carried out in a fixed-bed reactor with a diameter of 8 mm. The gas mixture consisted of 500 ppm NO, 500 ppm $NH_3$, 5.0 vol% $O_2$ and balance $N_2$. In all experiments, the total gas flow rate was maintained at 500 mL $min^{-1}$, corresponding to a gas hourly space velocity (GHSV) of 62 000 $h^{-1}$. The reaction temperatures were controlled regulated from 100 to 300 °C. The concentrations of NO and $O_2$ in the inlet and outlet gases were continually measured on-line by a flue gas analyzer (MRU VARIO PLUS, Germany).

### 2.3 Characterization

The morphologies and microstructures of the samples were examined using scanning electron microscope (SEM, FEI Nova NanoSEM 450) and transmission electron microscopy (TEM, JEOL JEM-2100F). The pore structure was measured at 77 K using a Quadrasorb SI analyzer (Quantachrome Instrument Crop) and the corresponding pore size distribution was obtained by the density functional theory (DFT model). X-ray diffraction (XRD) measurements were recorded on a Rigaku D/max 2550 diffractometer using Cu Kα radiation. X-ray photoelectron spectroscopy (XPS) measurements were carried out on an Axis Ultra DLD spectrometer with Al Kα radiation. $NH_3$-temperature programmed desorption ($NH_3$-TPD) was performed on a TP-5080 adsorption analyzer (Xianquan Co.) with a thermal conductivity detector (TCD). Before the $NH_3$-TPD experiment, 0.1 g sample was pretreated in He flow at 300 °C for 30 min, followed by cooling down to 100 °C. Afterwards, the He flow was switched to a stream containing 5 vol% $NH_3$/He to adsorb $NH_3$ for 60 min at 100 °C and then purged with He at the same temperature. Finally, the temperature was increased to 800 °C in He flow at a heating rate of 10 °C $min^{-1}$.

## 3. Results and discussion

### 3.1 Morphological characterization

Fig. 1 shows SEM images of the porous $SiO_2$ nanorods. As can be observed in Fig. 1, the obtained $SiO_2$ nanorods shows one-

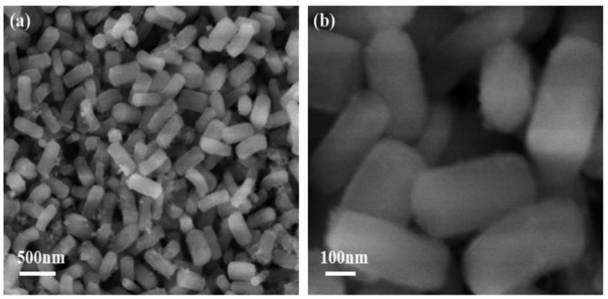


Fig. 1 SEM images of the porous $SiO_2$ nanorods.

dimensional rod-like structure. These nanorods are nearly uniform with lengths in the range of 300–400 nm and diameters of about 100–200 nm. Furthermore, all $SiO_2$ nanorods are almost monodispersed without aggregation.

The morphologies and microstructures of $MnO_x$ nanorods catalysts prepared by different methods are characterized by SEM. The results in Fig. 2 indicate the different morphology can be clearly observed over $MnO_x$(0.36)-E and $MnO_x$(0.36)-P nanorods. After the loading of $MnO_x$ and etching by the NaOH solution, the morphology of $MnO_x$(0.36)-E nanorods is mainly one-dimensional rod-like structure, which does not change much compared with that of $SiO_2$ nanorods. These indicate that $MnO_x$ is uniformly distributed in the rod-like structure, favorable to the enhancement of SCR activity. Additionally, a small amount of nanoparticles and nanosheets $MnO_x$ are observable on the surface of the rod-like structure, which may be caused by the unloaded $MnO_x$ on the $SiO_2$ nanorods because of the precipitation and crystallization of partial manganese precursor during the solvent evaporation process. The SEM image of $MnO_x$(0.36)-P nanorods is clearly different from that of $MnO_x$(0.36)-E nanorods. Flower-like structure is observed, which is assembled by numerous manganese oxide nanosheets (Fig. 2c and d). After the careful observation, it is found that a certain amount of loose macroporous structure is also formed on the surface of the catalyst, due to the accumulation of $MnO_x$ nanosheets. These macroporous structure could facilitate the adsorption and desorption of reactant gas molecules on the active sites of catalyst surface, which is advantageous to $NH_3$-SCR reaction.

The detailed morphologies and microstructures of $MnO_x$ nanorods catalysts obtained by different methods are further characterized by TEM. From Fig. 3a, it is observed that $MnO_x$(0.36)-E nanorods still maintains one-dimensional rod-like structure, agreeing well with the SEM results. It is worth noting that the inter center of $MnO_x$(0.36)-E nanorods is not completely hollow structure. Since the porous $SiO_2$ nanorods has abundant mesoporous structures, it is reasonable to expect

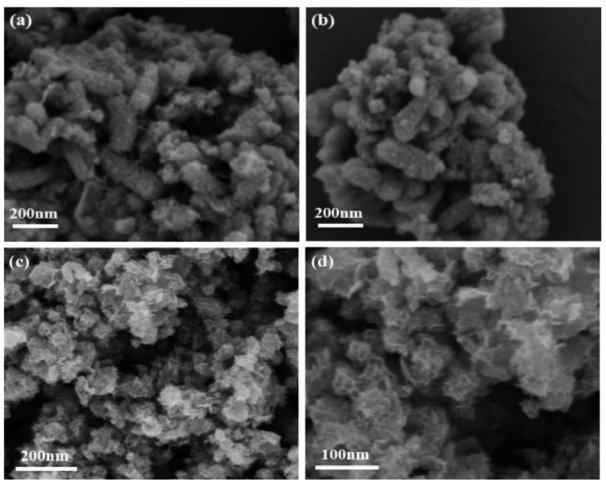


Fig. 2 SEM images of (a and b) $MnO_x$(0.36)-E and (c and d) $MnO_x$(0.36)-P nanorods catalysts.

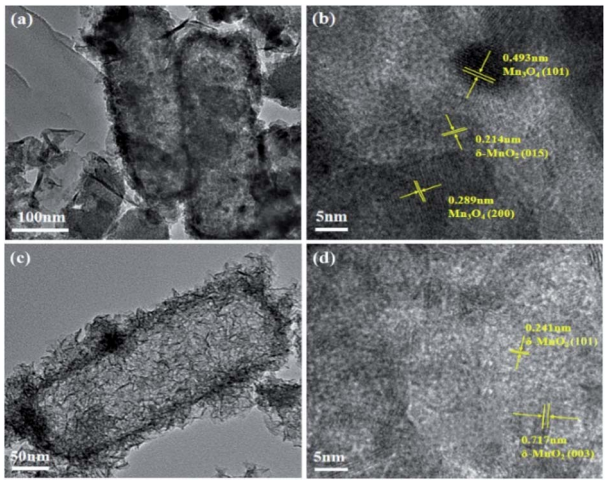


Fig. 3 TEM and HRTEM images of (a and b) $MnO_x$(0.36)-E and (c and d) $MnO_x$(0.36)-P nanorods.

the manganese precursor easily fills the mesoporous template including the edge and inner pores of $SiO_2$ nanorods during the $MnO_x$ impregnation process. Thus, the inner partially hollow structure is formed after the further etching of $SiO_2$. In addition, there exists unloaded nanoparticles and nanosheets $MnO_x$ near the rod-like structure, in accordance with the SEM results (Fig. 2a and b). Compared to TEM image of $MnO_x$(0.36)-E nanorods, $MnO_x$(0.36)-P nanorods is mainly composed of nanorods, with a diameter about 100–200 nm and length about 300–500 nm (Fig. 3c), which is similar with the size of the $SiO_2$ nanorods. And it can also be seen that $MnO_x$ nanosheets are deposited on the surface of the nanorods, suggesting that the flower-like $MnO_x$ is assembled by these $MnO_x$ nanosheets. Meanwhile, many porous structures in the inner space of nanorods are also observed, which is explained because the $MnO_x$ nanosheets are self-assembled randomly and not parallel to each other, leading to the formation of the porous structure. Such results are good agreement with the SEM observation (Fig. 2c and d).

The HRTEM images of the two catalysts are shown in Fig. 3b and d. The HRTEM image of $MnO_x$(0.36)-E nanorods reveals the visible lattice fringes with an interplanar spacing of 0.214, 0.289 and 0.493 nm, which can be assigned to the (015) plane of birnessite-type $MnO_2$ (δ-$MnO_2$), (200) and (101) planes of $Mn_3O_4$, respectively. These data suggests that $Mn_3O_4$ and δ-$MnO_2$ coexist on the surface of $MnO_x$(0.36)-E nanorods. However, for $MnO_x$(0.36)-P nanorods, the lattice fringes with an interplanar spacing of 0.241 and 0.717 nm can be observed, which can be assigned to the (101) and (003) crystal planes of δ-$MnO_2$, respectively.

### 3.2 NO removal activities

Fig. 4 exhibits the NO removal activities of $MnO_x$ nanorods catalysts obtained by the two different methods. It can be seen that the catalysts preparation method has significant effect on the NO removal activity. As shown in Fig. 4a, $MnO_x$(0.36)-P and $MnO_x$(0.72)-P nanorods catalysts exhibit higher NO removal

activity, above 94% of NO conversions can be achieved at temperatures of 100–200 °C. Especially in the low temperature range of 100–180 °C, they maintain about 98% NO conversions. For $MnO_x$(0.18)-P nanorods, it shows relatively low NO removal activity, but the maximum NO conversion is still up to 92% at 160 °C. From Fig. 4b, it can be observed that $MnO_x$(0.18)-E and $MnO_x$(0.36)-E nanorods catalysts exhibit relatively high NO removal activity. NO conversions of the two catalysts at 100 °C is approximately 70%, and they reach more than 90% in the temperature range of 140–240 °C. For $MnO_x$(0.72)-E nanorods, it shows relatively low NO removal activity below 200 °C, but it reaches a maximum value (above 90%) at 240 °C. For all $MnO_x$ nanorods, NO conversions decline at relative higher temperatures, which might be explained that partial $NH_3$ reductant is oxidized into NO.[18] Fig. 4c and d compare the NO removal activities over the $MnO_x$ nanorods catalysts obtained by the two different methods. Compared with $MnO_x$(0.36)-E nanorods, $MnO_x$(0.36)-P nanorods exhibits higher NO conversion in the low temperature range of 100–160 °C. For the catalyst with higher Mn loading, NO conversion of $MnO_x$(0.72)-P nanorods at low temperatures of 100–180 °C is significantly higher than that of $MnO_x$(0.72)-E nanorods. These results clearly indicate that the catalyst prepared by redox precipitation method shows much higher NO removal activity at the low temperature range (below 200 °C) than that prepared by solvent evaporation method, which may result from the unique morphology of $MnO_x$-P nanorods.

### 3.3 XRD

To further investigate the crystal phase composition of $MnO_x$ nanorods catalysts obtained by different methods, XRD patterns were characterized, and the results are shown in Fig. 5. The XRD pattern of $MnO_x$(0.36)-E nanorods displays the characteristic diffraction peaks located at $2\theta = 18.0°$, 28.9°, 32.4°, 36°, 44.4°, 58.5°, 59.9° and 64.7°, which can be indexed as the (101), (112), (103), (211), (220), (321), (224) and (400) crystal planes of $Mn_3O_4$ with a spinel structure (JCPDS card no. 24-0734), respectively.[19] And it can also be observed that the diffraction peaks at 12.3°, 24.8°, 36.9° and 42.2° are ascribed to the (003), (006), (101), and (015) crystal planes of δ-$MnO_2$ (JCPDS card no. 52-0556), respectively.[20] For $MnO_x$(0.36)-P nanorods, the diffraction peaks at 12.3°, 24.8°, 36.9°, 42.2°, and 66.3° are assigned to the (003), (006), (101), (015), and (113) planes of δ-$MnO_2$ crystalline phase. These data is consistent with the observation using HRTEM. It is worth noting that the diffraction peaks of $MnO_x$ on $MnO_x$(0.36)-P nanorods become broader and the intensities of the peaks become much weaker than those of $MnO_x$(0.36)-E nanorods, suggesting the smaller size of crystal particle and lower crystallinity of $MnO_x$. It has been widely demonstrated that amorphous phase of manganese oxides usually exhibits higher catalytic activity for SCR of NO

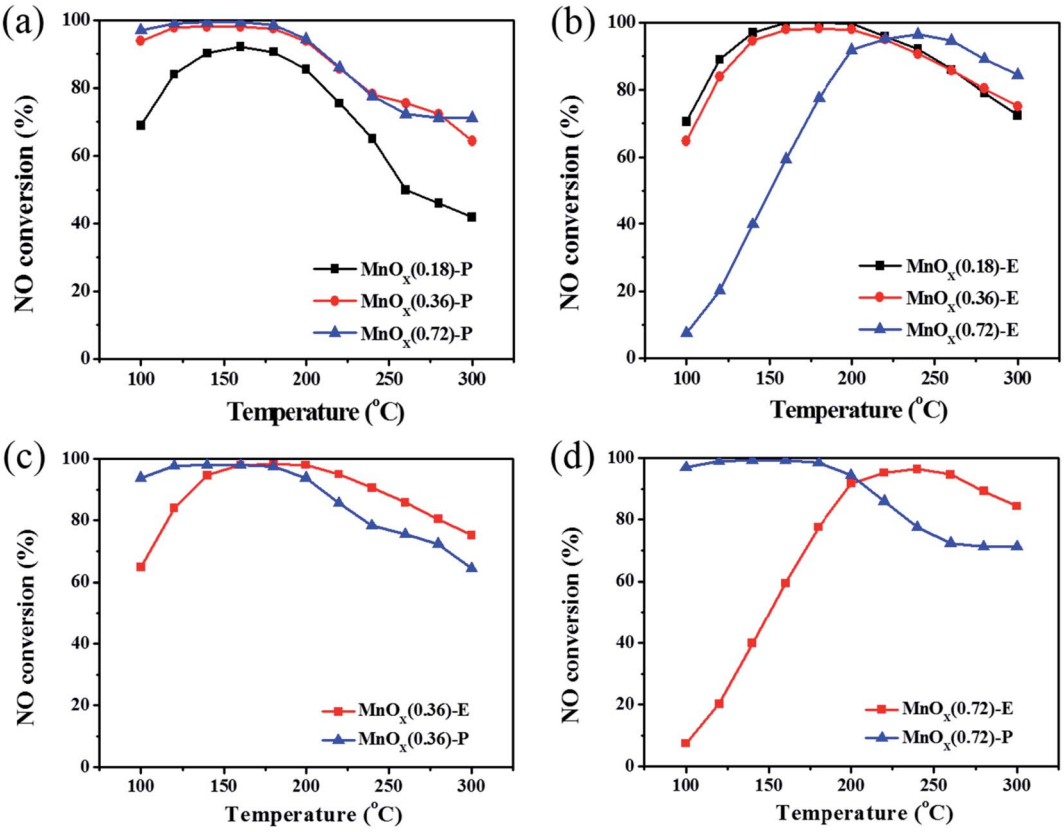


Fig. 4 NO conversions over the $MnO_x$ nanorods catalysts prepared by different methods. (a) $MnO_x$-P nanorods, (b) $MnO_x$-E nanorods, (c) $MnO_x$(0.36)-P and $MnO_x$(0.36)-E nanorods, (d) $MnO_x$(0.72)-P and $MnO_x$(0.72)-E nanorods.

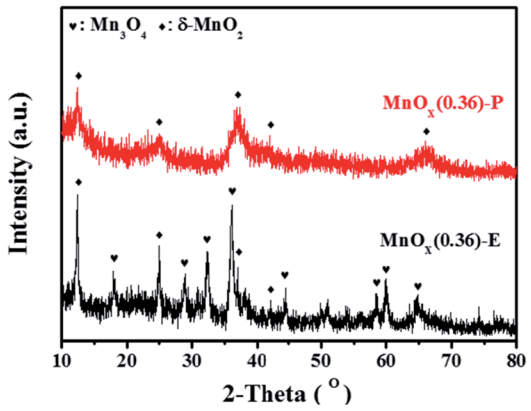


Fig. 5 XRD patterns of the different samples.

than crystal manganese oxides.[21] Based on these results, it can be concluded that the improved dispersion of $MnO_x$ species is obtained by the redox precipitation method, which contributes to the excellent SCR activity of $MnO_x$(0.36)-P nanorods, as evidenced by the results of activity evaluation presented in Fig. 4.

### 3.4 Pore structure analysis

The pore structure characterizations of the $MnO_x$ nanorods catalysts obtained by different methods are analyzed by $N_2$ adsorption–desorption isotherms. As presented in Fig. 6a, $MnO_x$(0.36)-E nanorods exhibits a typical type-IV isotherm with a hysteresis loop at the relative pressure ($P/P_0$) of 0.4–0.9, indicating the presence of mesopores. For $MnO_x$(0.36)-P nanorods, the isotherm still belongs to the type-IV isotherm with an obvious hysteresis loop at $P/P_0$ of 0.8–1.0, suggesting that the catalyst has characteristic of mesoporous material (Fig. 6c). Their pore sizes are further analyzed, as shown in Fig. 6b and d, respectively. The pore size distribution curve of $MnO_x$(0.36)-E nanorods shows the coexistence of micropores and mesopores, and its pore size distributes in the range of 0.6–4 nm. $MnO_x$(0.36)-P nanorods exhibits a wider pore size distribution and a larger number of mesopores in the range of 4–28 nm can be also observed. Moreover, the pore parameters of the samples are listed in Table 1. It can be observed that the $S_{BET}$ for $MnO_x$(0.36)-P and $MnO_x$(0.36)-E nanorods is 151 $m^2\ g^{-1}$ and 272 $m^2\ g^{-1}$, respectively. The $S_{BET}$ values of these $MnO_x$ nanorods catalysts are much larger than those of carrier-free $MnO_x$-based catalysts as previously reported,[15,22] which may result from the highly porous structure of $SiO_2$ nanorods template and/or the accumulation of the nanoparticles. It is worth pointing out that the $V_{total}$ of $MnO_x$(0.36)-P nanorods (0.61 $cm^3\ g^{-1}$) is significantly higher than that of $MnO_x$(0.36)-E nanorods (0.31 $cm^3\ g^{-1}$), which may be due to its flower-like structure, as demonstrated by the SEM results (Fig. 2c and d). Additionally, the pore volume of $MnO_x$(0.36)-P nanorods at smaller pore sizes (<4 nm) decreases obviously, and the pore volume at larger pore sizes (5–28 nm) increases greatly, indicating that there exists more mesoporous structure in $MnO_x$(0.36)-P nanorods. Thus, such rich mesoporous structure with high pore volume of $MnO_x$(0.36)-P nanorods may be favorable for exposure of more active sites of $MnO_x$ and the adsorption of reactant molecules, leading to the excellent SCR activity at the low temperatures (below 200 °C).

### 3.5 XPS characterization

To further determine the surface chemical states of elements in $MnO_x$ nanorods catalysts, the XPS measurement was carried out and the results are presented in Fig. 7. The relative atomic ratios of Mn and O elements are summarized in Table 2. As displayed Fig. 7a, the Mn 2p spectrum of $MnO_x$(0.36)-E nanorods exhibits two main peaks with binding energies of 653.8 eV and 642.3 eV, which represents Mn $2p_{1/2}$ and Mn $2p_{3/2}$, respectively. The Mn $2p_{3/2}$ spectrum can be fitted into three characteristic peaks at 641.0–642.0 eV, 642.2–642.5 eV and 642.9–643.7 eV, corresponding to $Mn^{2+}$, $Mn^{3+}$, and $Mn^{4+}$, respectively.[23,24] These data suggests that $Mn^{4+}$, $Mn^{3+}$ and $Mn^{2+}$ manganese oxide phases coexist on the surface of $MnO_x$(0.36)-E nanorods. For $MnO_x$(0.36)-P nanorods, the binding energies of Mn $2p_{1/2}$ and Mn $2p_{3/2}$ are located at 653.9 eV and 642.2 eV, respectively. The binding energy separation between these two peaks is 11.7 eV, which is in accordance with previously reported results of $MnO_2$,[25,26] indicating that the valence of Mn element is very close to 4 in $MnO_x$(0.36)-P nanorods. Moreover, the Mn $2p_{3/2}$ spectrum is fitted into two peaks, which are attributed to $Mn^{3+}$ (642.1 eV) and $Mn^{4+}$ (643.5 eV), respectively. These results further demonstrate that $MnO_2$ is the main manganese oxide in $MnO_x$(0.36) nanorods, which is in accordance with the XRD result. The relative ratio of different oxidation state of manganese species can be calculated by the area ratio of $Mn^{2+}$, $Mn^{3+}$ and $Mn^{4+}$ species, as shown in Table 2. The percentage of $Mn^{4+}$/$Mn^{n+}$ on $MnO_x$(0.36)-P nanorods (50.8%) is greatly higher than that on $MnO_x$(0.36)-E nanorods (35.7%). As literature reported,[27,28] manganese species with higher oxidation state are preferable for oxidation reactions over the manganese-based catalysts. It has been confirmed that $Mn^{4+}$ species are beneficial to promote the low-temperature SCR activity, due to the enhancement of oxidation of NO to $NO_2$.[29,30] Therefore, the higher percentage of $Mn^{4+}$ on $MnO_x$(0.36)-P nanorods results in the increased SCR activity at the low temperatures of 100–160 °C.

As shown in Fig. 7b, the O 1s XPS spectra can be fitted into two peak. The peak located at 529.5–530.2 eV can be assigned to the lattice oxygen ($O^{2-}$) (denoted as $O_\alpha$), while the peak located at 531.2–532.0 eV is assigned to the chemisorbed oxygen, such as $O^-$ or $O_2^{2-}$ (denoted as $O_\beta$).[31] The relative concentrations of $O_\alpha$ and $O_\beta$ can be determined from the area ratio of $O_\alpha/(O_\alpha + O_\beta)$ and $O_\beta/(O_\alpha + O_\beta)$, respectively. As illustrated by Table 2, the ratio of $O_\beta/(O_\alpha + O_\beta)$ is 49.3% and 38.6% for $MnO_x$(0.36)-E and $MnO_x$(0.36)-P nanorods, respectively, which is higher than the data previously reported for $MnO_2$ nanorods (36.7%) and $MnO_x$/$TiO_2$-GE (19.9%).[32,33] It has been widely reported that the surface chemisorbed oxygen species ($O_\beta$) are more active than the lattice oxygen species ($O_\alpha$) in oxidation reactions because of their higher mobility, which may easily exchange with oxygen in the gas phase or oxygen molecules absorbed on catalyst surface, thus acting as the supplement of lattice oxygen.[34–36] Moreover,

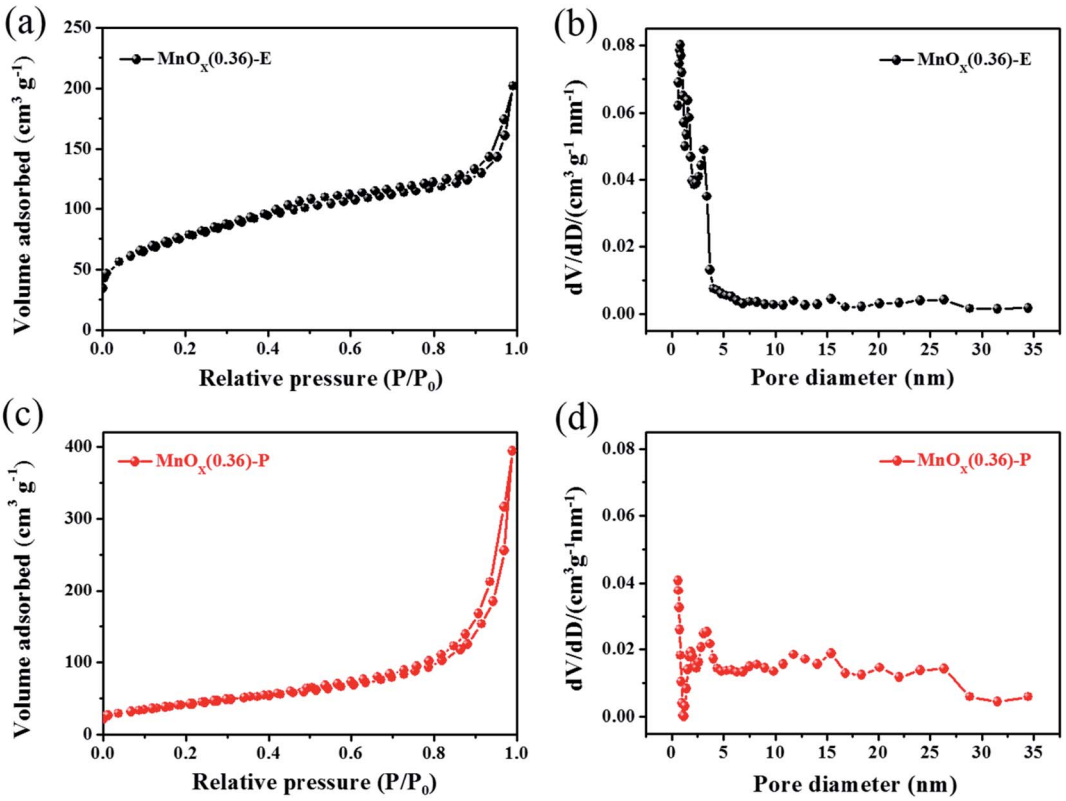


Fig. 6 $N_2$ adsorption–desorption isotherms and corresponding pore size distributions of (a and b) $MnO_x$(0.36)-E and (c and d) $MnO_x$(0.36)-P nanorods.

Table 1 Pore parameters of $MnO_x$ nanorods catalysts obtained by different methods[a]

| Sample | $S_{BET}$ ($m^2$ $g^{-1}$) | $V_{total}$ ($cm^3$ $g^{-1}$) | Average pore size (nm) |
|---|---|---|---|
| $MnO_x$(0.36)-P | 151 | 0.61 | 3.5 |
| $MnO_x$(0.36)-E | 272 | 0.31 | 4.6 |

[a] $S_{BET}$: BET specific surface area; $V_{total}$: total pore volume.

the higher concentration of $O_\beta$ is advantageous to the improvement of oxidation of NO to $NO_2$, which facilitates the "fast SCR" reaction ($4NH_3 + 2NO + 2NO_2 \rightarrow 4N_2 + 6H_2O$),[37–39] resulting in the enhancement of catalytic activity. Thus, the relative high concentration of surface chemisorbed oxygen in $MnO_x$(0.36)-E and $MnO_x$(0.36)-P nanorods is favorable for achieving high SCR activity. The above XPS results demonstrate that the high concentration of $Mn^{4+}$ species plays an important role in the low-temperature SCR activity of $MnO_x$(0.36)-P nanorods.

### 3.6 $NH_3$-TPD

It is generally known that the adsorption and oxidation of $NH_3$ on the surface acid sites of catalyst are considered to be a key step in the $NH_3$-SCR reaction. $NH_3$-TPD experiments were performed to determine the surface acidity of the obtained catalysts, and the results are shown in Fig. 8 and Table 3. It is found

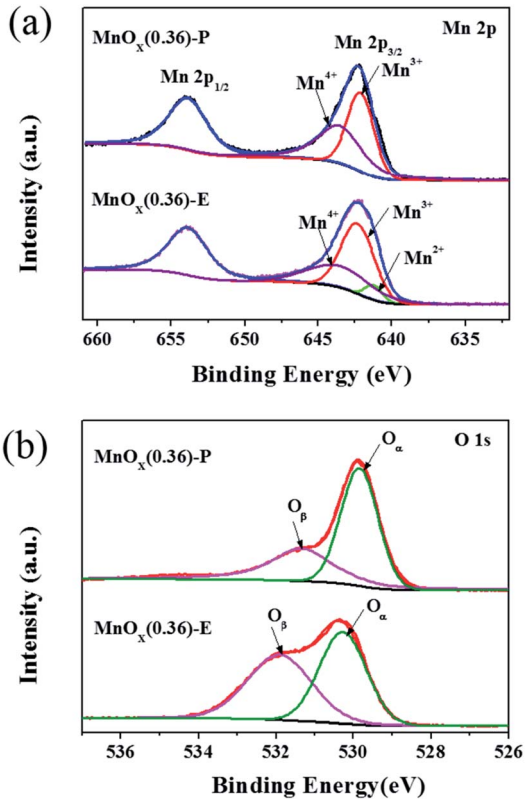


Fig. 7 XPS spectra for Mn 2p (a) and O 1s (b) of the different $MnO_x$ nanorods catalysts.

Table 2 The relative atomic ratios of the different $MnO_x$ nanorods catalysts

| | $X_{Mn}$ (%) | | | $X_O$ (%) | |
|---|---|---|---|---|---|
| Sample | $Mn^{2+}$ | $Mn^{3+}$ | $Mn^{4+}$ | $O_\alpha$ | $O_\beta$ |
| $MnO_x$(0.36)-P | 0 | 49.2 | 50.8 | 61.4 | 38.6 |
| $MnO_x$(0.36)-E | 6.4 | 57.9 | 35.7 | 50.7 | 49.3 |

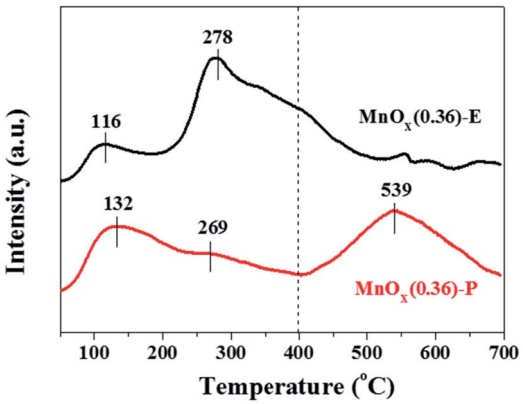


Fig. 8 $NH_3$-TPD profiles of the different $MnO_x$ nanorods catalysts.

Table 3 The amount of surface acids over the different catalysts

| | Peak temperature (°C) | | | Acid amount (a.u. $g^{-1}$) | | |
|---|---|---|---|---|---|---|
| Sample | $T_1$[a] | $T_2$ | $T_3$ | $S_1$[b] | $S_2$ | $S_3$ |
| $MnO_x$(0.36)-P | 132 | 269 | 539 | 30.3 | 28.9 | 56.7 |
| $MnO_x$(0.36)-E | 116 | 278 | — | 17.0 | 86.8 | — |

[a] The desorption peak at temperature. [b] The area of desorption peak.

that $MnO_x$(0.36)-E nanorods exhibits two obvious desorption peaks located at the temperature range of 50–180 °C (labeled as peak 1) and 190–400 °C (labeled as peak 2). And no visible desorption peaks above 400 °C can be observed. For $MnO_x$(0.36)-P nanorods, besides the two desorption peaks located at 50–400 °C, another desorption peak at 410–690 °C (labeled as peak 3) is also observed. The peaks 1 and 2 are ascribed to $NH_3$ desorption from the weak acid sites, and peak 3 is assigned to the strong acid sites. It is generally accepted that the area of $NH_3$ desorption peak is proportional to the amount of acid sites. As listed in Table 3, the desorption peak area of strong acid sites over $MnO_x$(0.36)-P nanorods significantly enhances compared with $MnO_x$(0.36)-E nanorods, indicating that a large amount of strong acid sites exist on its surface. Based on the above results, $MnO_x$(0.36)-P nanorods has stronger surface acidity, especially there are more amount of strong acid sites on it, which contributes to enhancement of $NH_3$ adsorption and oxidation on the catalyst surface, leading to the excellent low-temperature SCR activity of $MnO_x$(0.36)-P nanorods.

# 4. Conclusions

A series of $MnO_x$ nanorods catalysts using porous $SiO_2$ nanorods as template were synthesized through two different preparation methods. The obtained $MnO_x$-P nanorods catalyst prepared by redox precipitation method exhibits higher NO removal activity at low temperatures (lower than 200 °C) in comparison to $MnO_x$-E nanorods. About 98% NO conversion is achieved over $MnO_x$(0.36)-P nanorods in the low temperature range of 100–180 °C. The reason is mainly attributed to its unique flower-like morphology and mesoporous structures with high pore volume. Furthermore, there are the lower crystallinity of $MnO_x$, higher percentage of $Mn^{4+}$ species and a large amount of strong acid sites on the surface of $MnO_x$(0.36)-P nanorods. These factors result in its excellent low-temperature SCR activity.

## Conflicts of interest

There are no conflicts to declare.

## Acknowledgements

The authors gratefully acknowledge the financial supports from the National Natural Science Foundation of China (No. 51472086, 51002051, 22075081, 20806024), and the Natural Science Foundation of Shanghai City (12ZR1407200).

## Notes and references

1 S. B. Kristensen, A. J. Kunov-Kruse, A. Riisager, S. B. Rasmussen and R. Fehrmann, *J. Catal.*, 2011, **284**, 60–67.
2 P. Forzatti, *Catal. Today*, 2000, **62**, 51–65.
3 J. W. Shi, Z. Y. Fan, C. Gao, G. Gao, B. R. Wang, Y. Wang, C. He and C. M. Niu, *ChemCatChem*, 2018, **10**, 2833–2844.
4 J. Liu, Y. J. Wei, P. Z. Li, P. P. Zhang, W. Su, Y. Sun, R. Q. Zou and Y. L. Zhao, *ACS Catal.*, 2018, **8**, 3865–3874.
5 Y. R. Shi, X. L. Tang, H. H. Yi, F. Y. Gao, S. Z. Zhao, J. G. Wang, K. Yang and R. C. Zhang, *Ind. Eng. Chem. Res.*, 2019, **58**, 3606–3617.
6 C. Fang, D. S. Zhang, S. X. Cai, L. Zhang, L. Huang, H. R. Li, P. Maitarad, L. Y. Shi, R. H. Gao and J. P. Zhang, *Nanoscale*, 2013, **5**, 9199–9207.
7 R. H. Wang, Z. F. Hao, Y. Li, G. Q. Liu, H. Zhang, H. T. Wang, Y. G. Xia and S. H. Zhan, *Appl. Catal., B*, 2019, **258**, 117983.
8 F. Kapteijn, L. Singoredjo, A. Andreini and J. A. Moulijn, *Appl. Catal., B*, 1994, **3**, 173–189.
9 X. Y. Wang, K. Zhang, W. T. Zhao, Y. Y. Zhang, Z. X. Lan, T. H. Zhang, Y. H. Xiao, Y. F. Zhang, H. Z. Chang and L. L. Jiang, *Ind. Eng. Chem. Res.*, 2017, **56**, 14980–14994.
10 X. J. Yao, L. Chen, J. Cao, F. M. Yang, W. Tan and L. Dong, *Ind. Eng. Chem. Res.*, 2018, **57**, 12407–12419.
11 Z. H. Lian, W. P. Shan, Y. Zhang, M. Wang and H. He, *Ind. Eng. Chem. Res.*, 2018, **57**, 12736–12741.
12 S. H. Zhan, H. Zhang, Y. Zhang, Q. Shi, Y. Li and X. J. Li, *Appl. Catal., B*, 2017, **203**, 199–209.
13 C. L. Xiao, X. Y. Zhang, T. Mendes, G. P. Knowles, A. Chaffee and D. R. MacFarlane, *J. Phys. Chem. C*, 2016, **120**, 23976–23983.

14 C. Fang, L. Y. Shi, H. R. Li, L. Huang, J. P. Zhang and D. S. Zhang, *RSC Adv.*, 2016, **6**, 78727–78736.
15 J. S. Gao, Y. L. Han, J. C. Mu, S. C. Wu, F. Tan, Y. Shi and X. Y. Li, *J. Colloid Interface Sci.*, 2018, **516**, 254–262.
16 W. Tian, H. S. Yang, X. Y. Fan and X. B. Zhang, *J. Hazard. Mater.*, 2011, **188**, 105–109.
17 W. Q. Yao, C. J. Chu, W. Z. Zheng, L. Zhan and Y. L. Wang, *J. Mater. Chem. A*, 2018, **6**, 18191–18205.
18 T. S. Park, S. K. Jeong, S. H. Hong and S. C. Hong, *Ind. Eng. Chem. Res.*, 2001, **40**, 4491–4495.
19 Y. F. Jian, M. D. Ma, C. W. Chen, C. Liu, Y. K. Yu, Z. P. Hao and C. He, *Catal. Sci. Technol.*, 2018, **8**, 3863–3875.
20 G. Zhu, L. J. Deng, J. F. Wang, L. P. Kang and Z. H. Liu, *Colloids Surf., A*, 2013, **434**, 42–48.
21 G. Gao, J. W. Shi, C. Liu, C. Gao, Z. Y. Fan and C. M. Niu, *Appl. Surf. Sci.*, 2017, **411**, 338–346.
22 S. H. Zhan, D. D. Zhu, M. Y. Qiu, H. B. Yu and Y. Li, *RSC Adv.*, 2015, **5**, 29353–29361.
23 Z. Y. Fan, J. W. Shi, C. Gao, G. Gao, B. R. Wang and C. M. Niu, *ACS Appl. Mater. Interfaces*, 2017, **9**, 16117–16127.
24 C. L. Li, X. L. Tang, H. H. Yi, L. F. Wang, X. X. Cui, C. Chu, J. Y. Li, R. C. Zhang and Q. J. Yu, *Appl. Surf. Sci.*, 2018, **428**, 924–932.
25 X. Wang, Y. Y. Zheng, Z. Xu, Y. Liu and X. L. Wang, *Catal. Sci. Technol.*, 2014, **4**, 1738–1741.
26 E. Miniach, A. Sliwak, A. Moyseowicz, L. Fernández-Garcia, Z. González, M. Granda, R. Menendez and G. Gryglewicz, *Electrochim. Acta*, 2017, **240**, 53–62.
27 X. F. Tang, Y. G. Li, X. M. Huang, Y. D. Xu, H. Q. Zhu, J. G. Wang and W. J. Shen, *Appl. Catal., B*, 2006, **62**, 265–273.
28 Q. Shen, L. Y. Zhang, N. N. Sun, H. Wang, L. S. Zhong, C. He, W. Wei and Y. H. Sun, *Chem. Eng. J.*, 2017, **322**, 46–55.
29 B. X. Shen, Y. Y. Wang, F. M. Wang and T. Liu, *Chem. Eng. J.*, 2014, **236**, 171–180.
30 L. Zhang, D. S. Zhang, J. P. Zhang, S. X. Cai, C. Fang, L. Huang, H. R. Li, R. H. Gao and L. Y. Shi, *Nanoscale*, 2013, **5**, 9821–9829.
31 K. W. Zha, S. X. Cai, H. Hu, H. R. Li, T. T. Yan, L. Y. Shi and D. S. Zhang, *J. Phys. Chem. C*, 2017, **121**, 25243–25254.
32 Y. Li, Y. P. Li, Y. Wan, S. H. Zhan, Q. X. Guan and Y. Tian, *RSC Adv.*, 2016, **6**, 54926–54937.
33 X. N. Lu, C. Y. Song, S. H. Jia, Z. S. Tong, X. L. Tang and Y. X. Teng, *Chem. Eng. J.*, 2015, **260**, 776–784.
34 F. D. Liu, W. P. Shan, Z. H. Lian, L. J. Xie, W. W. Yang and H. He, *Catal. Sci. Technol.*, 2013, **3**, 2699–2707.
35 P. Sun, R. T. Guo, S. M. Liu, S. X. Wang, W. G. Pan and M. Y. Li, *Appl. Catal., A*, 2017, **531**, 129–138.
36 L. Chen, X. X. Wang, Q. L. Cong, H. Y. Ma, S. J. Li and W. Li, *Chem. Eng. J.*, 2019, **369**, 957–967.
37 F. D. Liu, H. He, Y. Ding and C. B. Zhang, *Appl. Catal., B*, 2009, **93**, 194–204.
38 T. Boningari, P. R. Ettireddy, A. Somogyvari, Y. Liu, A. Vorontsov, C. A. McDonald and P. G. Smirniotis, *J. Catal.*, 2015, **325**, 145–155.
39 F. Y. Gao, X. L. Tang, H. H. Yi, J. Y. Li, S. Z. Zhao, J. G. Wang, C. Chu and C. L. Li, *Chem. Eng. J.*, 2017, **317**, 20–31.